

# A 3D Cu-Naphthalene-Phosphonate Metal–Organic Framework with Ultra-High Electrical Conductivity

Craig A. Peeples, Delf Kober, Franz-Josef Schmitt, Patrik Tholen, Konrad Siemensmeyer, Quinn Halldorson, Bünyemin Çoşut, Aleksander Gurlo, Ahmet Ozgur Yazaydin, Gabriel Hanna,\* and Gündoğ Yücesan\*

A conductive phosphonate metal–organic framework (MOF),  $[\{Cu(H_2O)\}_2(2,6\text{-NDPA})_{0.5}]$  (NDPA = naphthalenediphosphonic acid), which contains a 2D inorganic building unit (IBU) comprised of a continuous edge-sharing sheet of copper phosphonate polyhedra is reported. The 2D IBUs are connected to each other via polyaromatic 2,6-NDPA's, forming a 3D pillared-layered MOF structure. This MOF, known as TUB40, has a narrow band gap of 1.42 eV, a record high average electrical conductance of  $2 \times 10^2 \text{ S m}^{-1}$  at room temperature based on single-crystal conductivity measurements, and an electrical conductance of  $142 \text{ S m}^{-1}$  based on a pellet measurement. Density functional theory (DFT) calculations reveal that the conductivity is due to an excitation from the highest occupied molecular orbital on the naphthalene-building unit to the lowest unoccupied molecular orbital on the copper atoms. Temperature-dependent magnetization measurements show that the copper atoms are antiferromagnetically coupled at very low temperatures, which is also confirmed by the DFT calculations. Due to its high conductance and thermal/chemical stability, TUB40 may prove useful as an electrode material in supercapacitors.

conductive materials such as perovskites and graphene derivatives,<sup>[1–10]</sup> which possess limited structural diversity around their well-defined 2D layers. Recently, there has been a great deal of interest in creating novel conductive MOFs, as their surface areas can be modified using well-established reticular chemistry with longer tethered organic linkers to provide optimizable charge-holding capacities.<sup>[11–16]</sup> Such MOFs have the potential to be used as electrode materials in next-generation supercapacitors.<sup>[11,12]</sup>

Reticular MOF synthesis has evolved around the use of longer tethered linkers with molecular IBUs, which diminish the interactions between the IBUs.<sup>[17–20]</sup> In addition, the use of conventional carboxylic acid metal-binding units typically leads to larger band gaps above 2.5 eV.<sup>[21,22]</sup> The known conductive ortho-dimine,

ortho-dihydroxy, and azolate MOFs have conservative metal-binding modes, thereby limiting further developments of these systems.<sup>[13,14,16,23,24]</sup> Alternative metal-binding units with rich structural diversity and metal-binding modes that generate 1D or 2D IBUs spawning continuous interaction of metal polyhedra along the IBUs, have been known to introduce semi-conductive behavior in MOFs.<sup>[12,15,16]</sup> (Comprehensive tables of

## 1. Introduction

Metal organic frameworks (MOFs) are composed of inorganic building units (IBUs) that are linked together via organic struts or linkers. Owing to all the possible coordination combinations of inorganic and organic components, they exhibit extremely rich structural diversity compared to traditional 2D

C. A. Peeples, Q. Halldorson, Prof. G. Hanna  
Department of Chemistry  
University of Alberta  
Edmonton T6G 2R3, Canada  
E-mail: gabriel.hanna@ualberta.ca

D. Kober, Prof. A. Gurlo  
Institut für Werkstoffwissenschaften und Technologien  
Fachgebiet Keramische Werkstoffe  
Technische Universität  
Berlin 13355, Germany

 The ORCID identification number(s) for the author(s) of this article can be found under <https://doi.org/10.1002/adfm.202007294>.

© 2020 The Authors. Published by Wiley-VCH GmbH. This is an open access article under the terms of the Creative Commons Attribution-NonCommercial-NoDerivs License, which permits use and distribution in any medium, provided the original work is properly cited, the use is non-commercial and no modifications or adaptations are made.

The copyright line for this article was changed on 2 October 2020 after original online publication.

DOI: 10.1002/adfm.202007294

Dr. F.-J. Schmitt  
Department of Physics  
Marthin-Luther-Universität Halle-Wittenberg  
Halle (Saale) 06120, Germany

P. Tholen, Prof. G. Yücesan  
Department of Food Chemistry and Toxicology  
Technische Universität  
Berlin 13355, Germany  
E-mail: yuecesan@tu-berlin.de

Dr. K. Siemensmeyer  
Helmholtz-Zentrum  
Berlin 14109, Germany

Prof. B. Çoşut  
Department of Chemistry  
Gebze Technical University  
Gebze 41400, Turkey

Prof. A. O. Yazaydin  
Department of Chemical Engineering  
University College London  
London WC1E 7JE, UK

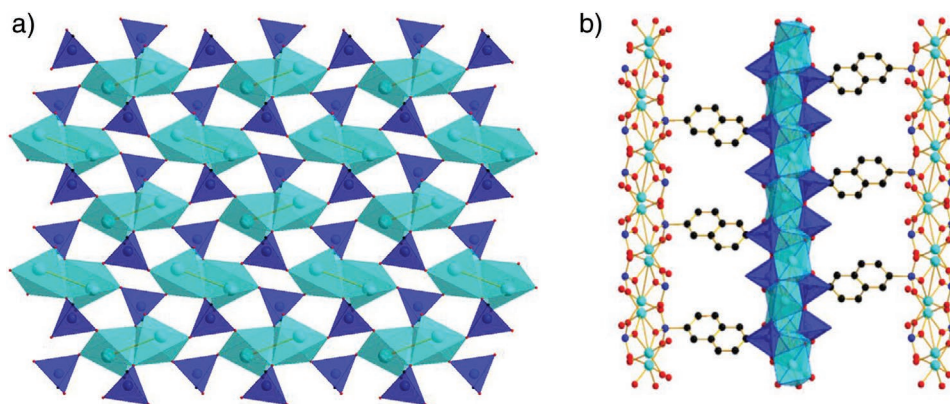
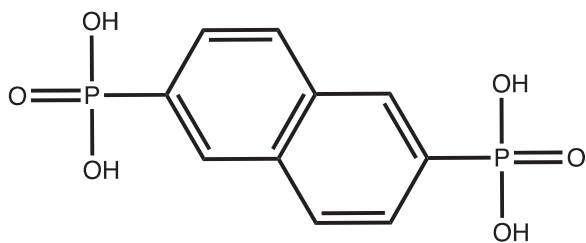


**Figure 1.** a) View of  $\{[\text{Cu}(\text{H}_2\text{O})]\text{(2,6-NDPA)}_{0.5}\}$  TUB40's 2D copper phosphonate IBU composed of edge-sharing Cu–O–P–O–Cu–O–P–O polyhedra (see Scheme 1 for the Lewis structure of 2,6-NDPA). b) Crystal structure of the 3D pillared-layered network of TUB40.

electrical conductivities of conductive MOFs may be found in a recent review article.<sup>[16]</sup> The same approach is also known to introduce magnetic interactions between the metal ions in the MOF structure.<sup>[15,25–27]</sup> Along these lines, organophosphonates are known to possess rich structural diversity and metal-binding modes<sup>[8,20,28–31]</sup> and readily form 1D and 2D IBUs under hydrothermal reaction conditions.<sup>[8]</sup> In a recent study,<sup>[15]</sup> we reported the first semiconductive and magnetic phosphonate MOF (known as TUB75) composed of 1D antiferromagnetically coupled Cu(II) dimer chains and 1,4-naphthalenediphosphonic acid linkers. We showed that the phosphonate polyhedra within the 1D IBU contributed to the electron delocalization throughout the IBU. In the current study, we revisit our previously published MOF TUB40,<sup>[32]</sup> which is composed of 2D sheets of corner-sharing copper and phosphorus polyhedra (see Figure 1 for a depiction of the 2D sheets and crystal structure of TUB40), and explore its conductive and magnetic properties. In particular, we perform pellet conductivity, single-crystal conductivity, solid-state diffuse reflectance (to estimate the band gap via Tauc plotting), temperature-dependent magnetization measurements, and density functional theory (DFT) calculations.

## 2. General Information

The presence of the tetrahedral  $\text{R-PO}_3\text{H}_2$  metal-binding unit in phosphonate MOFs leads to certain advantages over conventional MOFs.<sup>[28–31]</sup> The phosphonic acid functional group is known to have a high metal-binding affinity.<sup>[33–35]</sup> Since fully deprotonated, negatively (–2) charged phosphonates can form



**Scheme 1.** Lewis structure of 2,6-naphthalenediphosphonic acid (2,6-NDPA).

strong ionic bonds with divalent metal ions, phosphonate MOFs have high thermal and chemical stabilities.<sup>[36,37]</sup> TUB40 was previously reported to be thermally stable up till  $\approx 400^\circ\text{C}$ ,<sup>[32]</sup> as it is composed of fully deprotonated phosphonate moieties. In the absence of the coordinated water molecules, TUB40 is estimated to have a Helium-accessible specific pore volume of  $0.032\text{ cm}^3\text{ g}^{-1}$ , corresponding to a 7% v/v void fraction, based on a Monte Carlo simulation (see Supporting Information for details). TUB40 was synthesized as single-phase (pistachio-green) crystals under autogenic pressure in a 23-mL Teflon-coated Parr hydrothermal reaction vessel at  $180^\circ\text{C}$ .

## 3. Semiconducting and Magnetic Properties

### 3.1. Band Gap

CuO is known to be a good semiconductor with a band gap of 1.2 eV.<sup>[38]</sup> Based on our findings in ref. [15], it is presumed that the introduction of phosphonate groups throughout the copper oxide framework retains the semiconductivity in the 2D IBUs. In addition, the rich metal-binding modes found in phosphonate MOFs allows for optimizable surface areas, which could expand the range of semiconductor applications. Therefore, we sought to estimate the band gap of TUB40 from the UV–vis diffuse reflectance spectrum of handpicked crystals of TUB40. As seen in Figure 2a, indirect Tauc plotting of the reflectance data reveals a band gap of 1.42 eV, which lies in the semiconductive range.<sup>[39,40]</sup>

### 3.2. Pellet-Based Conductivity

Given the narrow bandgap, we then used impedance spectroscopy to measure the resistance of a 5 mm (diameter)  $\times$  0.5 mm (thickness) TUB40 pellet at room temperature and calculated the resulting electrical conductivity ( $\sigma$ ). This was done using a Zahner ZENNIUM impedance measurement unit in the potentiostatic mode (with 20 mV amplitude between 100 mHz and 100 kHz). To reduce the influence of contact resistance between the pellet surface and electrodes (stainless steel cylinders), the impedance measurement was done under a mechanical load of 1 MPa. In Figure 2b, the complex-valued impedance is

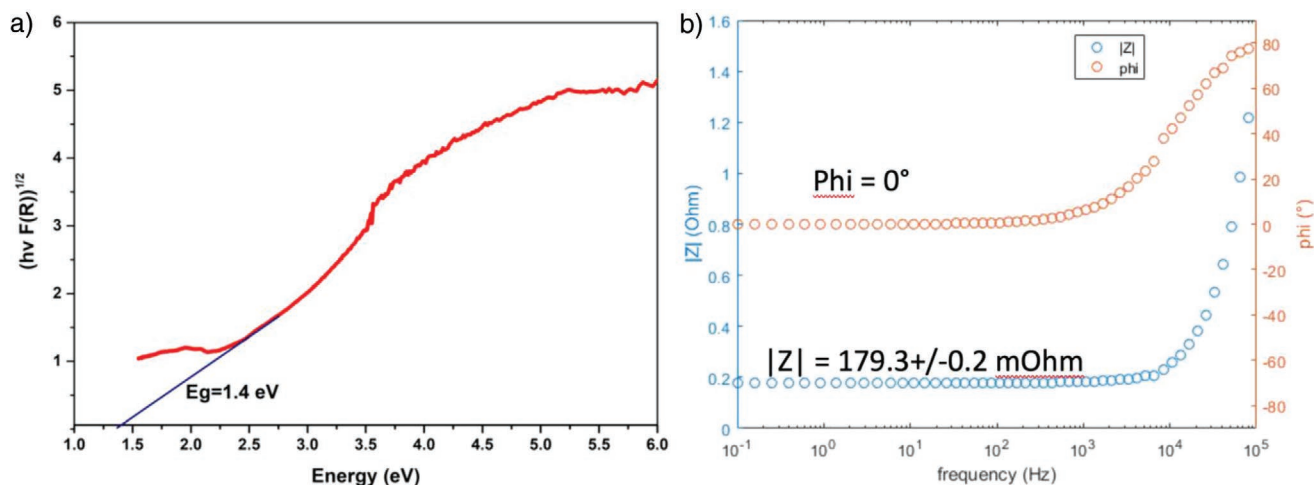


**Figure 2.** a) Tauc plot of UV-vis diffuse reflectance spectrum for TUB40, showing the indirect band gap of 1.4 eV. b) Impedance spectrum of TUB40 revealing purely ohmic behavior with  $|Z| = 179.3 \pm 0.2 \text{ m}\Omega$  between 0.1 and  $\approx 500 \text{ Hz}$ . Above  $\approx 500 \text{ Hz}$ ,  $|Z|$  and  $\phi$  increase due to the increasing parasitic contributions from the connectors and cables in the setup.

displayed in the Bode representation in terms of the magnitude of the impedance,  $|Z|$ , and the phase shift,  $\phi$ , between the input potential wave and measured current wave (NB:  $\phi = 0$  for ohmic resistors and  $\phi \neq 0$  for serial or parallel combinations of capacitive, inductive, and resistive elements). From 0.1 to  $\approx 500 \text{ Hz}$ , we see that  $|Z|$  and  $\phi$  remain constant at  $179.3 \pm 0.2 \text{ m}\Omega$  and  $0^\circ$ , respectively. This frequency independence is characteristic of pure ohmic resistors. Above  $\approx 500 \text{ Hz}$ , the plot exhibits a common feature of an impedance measurement setup, namely,  $\phi$  increases with increasing frequency toward  $90^\circ$  (here,  $80^\circ$  at  $100 \text{ kHz}$ ). This artifact is caused by parasitic contributions from the connectors and cables, which lead to measurable inductances due to mutual induction or object- and wiring-inductance. Thus, frequencies with  $\phi$  values higher than  $1^\circ$  were not considered in the calculation of the resistance,  $R$ , that is,  $R$  was calculated from the mean  $|Z|$  between 0.1 and  $200 \text{ Hz}$ . Finally, the conductivity,  $\sigma$ , was calculated to be

$$\sigma = \frac{l}{RA} = \frac{5 \times 10^{-4} \text{ m}}{0.1793 \Omega \cdot (0.25 \cdot \pi \cdot (5 \times 10^{-3} \text{ m})^2)} = 142 \text{ S m}^{-1} \quad (1)$$

### 3.3. Single-Crystal Conductivity

As measurements on polycrystalline pellets may underestimate the conductance of the MOF due to contact/grain boundary resistances and anisotropic electrical conduction, we also performed single-crystal measurements according to the setup described in ref. [15]. The TUB40 crystals were hand-picked under a microscope (see Figure S5, Supporting Information) and a number of measurements were performed by clamping the individual crystals in a flat alignment between two gold surfaces of a relay (see Supporting Information for more details). Assuming that the TUB40 crystal made perfect contact with the gold surfaces, the measured resistances yielded a maximum conductance of  $\approx 10^3 \text{ S m}^{-1}$  with an average of  $\approx 200 \text{ S m}^{-1}$ . Since the main crystal body is surrounded by smaller rectangular plates of TUB40 crystals (see Figure S5,

Supporting Information), perfect contact with the gold surfaces is probably not made and thus the reported average conductance may underestimate the actual average.

### 3.4. Magnetization Measurements

Temperature-dependent magnetization measurements of a 20 mg sample of TUB40 were conducted using a Squid-based vibrating sample magnetometer (MPMS by Quantum Design) in direct current mode. The magnetization data were obtained in a temperature range between 2 and 380 K for applied magnetic fields between 0.1 and 7 Tesla and the corresponding susceptibilities [calculated from the magnetization ( $M$ ) and applied magnetic field ( $B$ )] are shown in Figure 3a. For low applied fields up to 2 Tesla, the magnetic susceptibility shows a broad peak with a maximum at  $T_{\text{max}} \approx 4 \text{ K}$ , which is essentially independent of field strength. Such a result is consistent with short-range antiferromagnetic order in the 2D Cu planes.<sup>[41,42]</sup> For the higher applied field strengths, the peak maximum shifts to lower temperatures with increasing field strength due to the greater influence of the magnetic field over the short-range interactions. Above  $T_{\text{max}}$ , the susceptibility decays with increasing temperature to a small value at room temperature, indicative of paramagnetic behavior.

The inverse susceptibilities,  $\chi^{-1}$ , which are used to obtain Curie-Weiss fits of the data, are shown in Figure 3b. As can be seen, straight lines are only observed at high field strengths, with deviations observed at low field strengths, namely,  $\chi^{-1}(T)$  curves downward at high temperatures due to paramagnetic or ferromagnetic contributions. It should be noted that diamagnetic contributions, if present, would bend  $\chi^{-1}(T)$  upward at high temperatures and be field-independent. A good fit to the susceptibility,  $\chi$ , over the full temperature range from 10 K to the highest temperature was obtained using the following function:

$$\chi = C_{\text{CW}} / (T - \theta_{\text{CW}}) + \chi_{\text{dia}} + C_{\text{B}} / \sqrt{B} \quad (2)$$

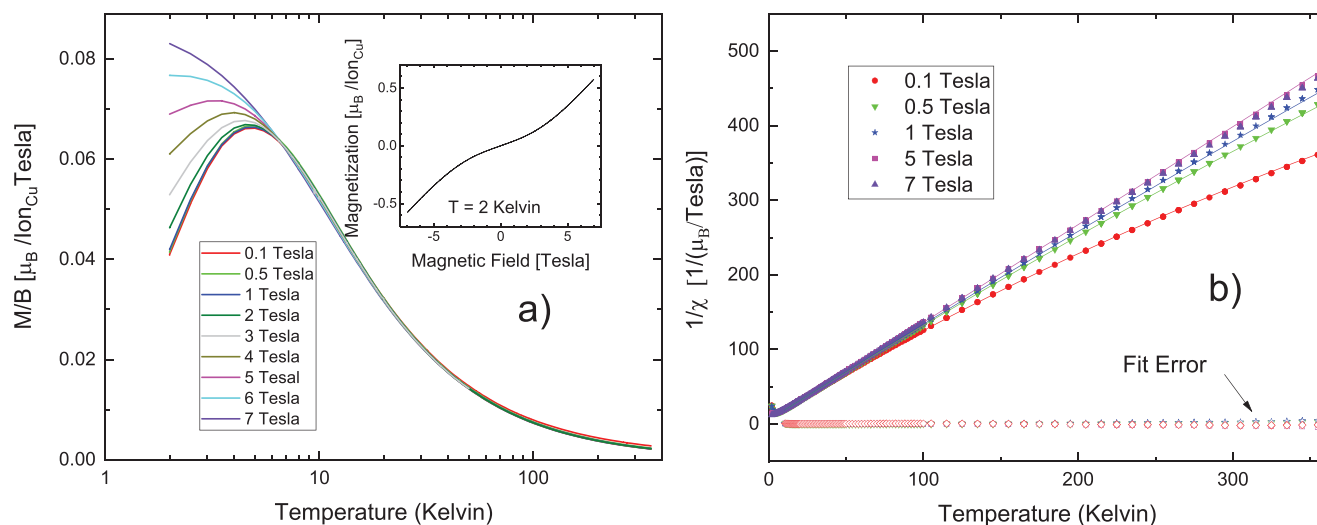


**Figure 3.** a) Magnetic susceptibility,  $M/B$ , as a function of temperature for different values of the applied magnetic field, as obtained from the raw magnetization data. The inset shows the magnetization as a function of the applied field at 2 K. b) Inverse susceptibility,  $1/\chi$ , (filled symbols) as a function of temperature for different values of the applied magnetic field, along with fits to the data (solid lines). The deviations between the fits and measured data are also shown (open symbols).

where  $C_{\text{CW}}$  and  $\Theta_{\text{CW}}$  are the Curie and Curie-Weiss constants, respectively, and  $\chi_{\text{dia}}$  is the diamagnetic contribution. The last field-dependent term,  $\chi_{\text{b}} = C_{\text{b}}/\sqrt{B}$ , is introduced to capture the deviations from the Curie-Weiss behavior observed at high temperatures, where  $C_{\text{b}}$  is a temperature-independent constant. The observed square root behavior can arise from a small amount of ferromagnetic impurity with soft magnetic properties.<sup>[43]</sup> The fit gives  $C_{\text{CW}} = 0.76 \mu_{\text{B}}\text{K}/\text{Ion}_{\text{Cu}}$  Tesla,  $\Theta_{\text{CW}} = -4.13$  K,  $\chi_{\text{dia}} = 110 \times 10^{-6} \mu_{\text{B}}/\text{Ion}_{\text{Cu}}$  Tesla, and  $C_{\text{b}} = 225 \times 10^{-6} \mu_{\text{B}}/\text{Ion}_{\text{Cu}} \sqrt{\text{Tesla}}$ . Assuming Cu spins with  $g = 2$ , the obtained value of the Curie constant,  $C_{\text{CW}}$ , suggests that  $\approx 80\%$  of the Cu spins per mole of spins contribute to the magnetic interactions. The field dependence of the magnetization at 2 K (see inset of Figure 3a) shows a change in slope at 2.5 Tesla to paramagnetic behavior. This value of the field corresponds to a Zeeman splitting of 3.4 K for Cu spins, which is consistent with  $T_{\text{max}} \approx 4$  K and  $\Theta_{\text{CW}} = -4.13$  K. The negative sign of the latter indicates that the interactions are antiferromagnetic. The magnitudes of the ferromagnetic ( $\chi_{\text{b}}$ ) and diamagnetic ( $\chi_{\text{dia}}$ ) backgrounds are very small compared to the low-temperature susceptibility values, so they can be safely treated within this fit. The diamagnetic background can arise from the non-magnetic atoms in TUB40.

#### 4. DFT Calculations

DFT calculations of the density of states (DOS), projected density of states (pDOS), band gap, band structure, and partial charges of TUB40 were also carried out. The details of the geometry optimization and DFT calculations can be found in the Supporting Information. **Figure 4** shows the optimized structure of the antiferromagnetic (AFM) configuration of TUB40 (the optimized structure of the ferromagnetic (FM) configuration is negligibly different). As seen in Table S1, Supporting Information, the structural differences between the optimized structure and experimental crystal structure are minimal. The exchange energy (i.e., difference between the

energies of the AFM and FM configurations) was calculated to be  $E_{\text{x}} = E_{\text{AFM}} - E_{\text{FM}} = -1.50$  meV, suggesting that the zero-temperature magnetic ground state is the AFM state (in agreement with the magnetic susceptibility data below 5 K).

We first present and discuss the HOMO-LUMO gap and pDOSs of the AFM configuration (the total DOS and band structure may be found in Figure S1, Supporting Information). The HOMO-LUMO gap was calculated to be 2.320 eV and, as seen in the pDOS (**Figure 5**), the HOMO is predominantly dictated by the carbon orbitals of the naphthalenes and the LUMO by the orbitals on the copper and, to a lesser extent, the oxygen atoms. These results suggest that the AFM configuration has a spatially separated HOMO-to-LUMO transition. Further insight into the HOMO-LUMO gap is provided by the pDOSs in **Figure 6**, which show the contributions from the p-orbitals of the carbon atoms and the d-orbitals of the copper atoms with excess  $\beta$  (**Figure 6A**) and  $\alpha$ -spins (**Figure 6B**). As can be seen,

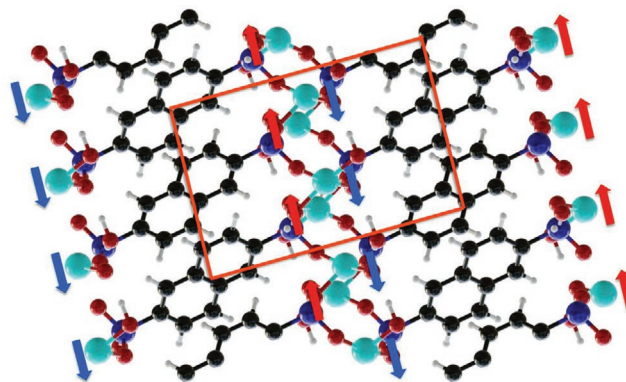


**Figure 4.** Minimum energy structure of the  $2 \times 1 \times 2$  supercell of TUB40 in the AFM configuration, obtained at the DZP-PBE-D3 level of theory. The orange box delineates the unit cell. The red and blue arrows denote the  $\alpha$  and  $\beta$  spins, respectively, of the unpaired electrons of the copper atoms. For the FM configuration, all of the unpaired electrons are taken to be spin- $\alpha$  (O – red; Cu – cyan; P – blue; C – black; H – white).

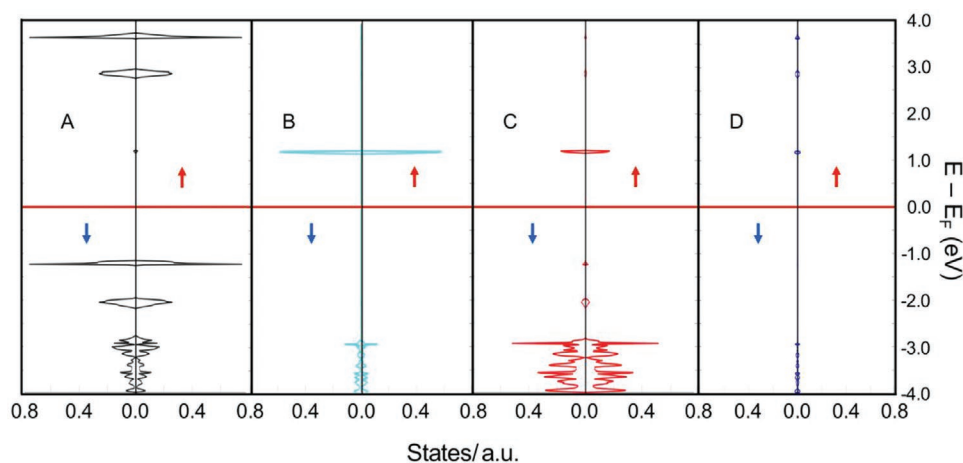


**Figure 5.** Spin-up (red arrow) and spin-down (blue arrow) projected density of states for TUB40 in the AFM configuration: carbon (A), copper (B), oxygen (C), phosphorous (D).

the spin orientations of the copper d-orbitals contributing to the LUMO depend on the copper atom under consideration (i.e., a copper atom with an excess  $\beta$ -spin or  $\alpha$ -spin). Specifically, for the copper atoms with the excess  $\beta/\alpha$ -spins, spin-up/down electrons may populate the copper d-orbitals of the LUMO. Due to the electronic transition selection rule that  $\Delta S = 0$  (i.e., the spin of the electron cannot change), our results suggest the possibility of excitations of spin-up/down electrons from the naphthalene  $\pi$  orbitals to the empty d-orbitals of copper atoms with unpaired spin-down/up electrons, that is, a copper atom with an unpaired spin-up electron will only accept an excited spin-down electron into its empty d-orbitals and vice versa.

Given the small exchange energy, we next present and discuss the HOMO-LUMO gaps and pDOSs of the FM configuration. Based on the spin-up and spin-down band gaps, band structure (Figure S2, Supporting Information), total DOS (Figure S2, Supporting Information), and pDOS (Figure 7), we see that the FM configuration's HOMO-LUMO gap is spin-dependent. More specifically, the spin-down states have a band gap of 2.195 eV, in the semiconductor regime, while the spin-up states have a band gap of 3.913 eV, which is closer to that of an insulator. This situation may be contrasted with that of a half-metal, where one spin orientation has a zero band gap and the other has

a non-zero band gap.<sup>[44–46]</sup> As can be seen in Figure S2, Supporting Information, the HOMO is spin-independent while the LUMO is spin-dependent. To understand how the various atoms contribute to the spin-dependent HOMO-LUMO gap, we calculated the pDOS for carbon, copper, oxygen, and phosphorous shown in Figure 7. The figure reveals that the HOMO of TUB40 in the FM configuration is predominantly dictated by the carbon orbitals of the naphthalenes (as in the case of the AFM configuration). On the other hand, the spin-down contribution to the LUMO is mainly composed of copper orbitals with a small contribution from the oxygen orbitals (as in the case of the AFM configuration), while the spin-up contribution is due to carbon orbitals. Based on these results, we see that the spin-down states have a spatially separated HOMO-to-LUMO transition (as in the case of the AFM configuration), while that of the spin-up states is localized on the naphthalene carbon atoms. Further insight into the HOMO-LUMO gap is provided by the pDOS in Figure 8, which shows the contributions from the p-orbitals of the carbon atoms and the d-orbitals of the copper atoms with excess  $\alpha$ -spins. As can be seen, spin-down electrons may populate the copper d-orbitals of the LUMO. Due to the electronic transition selection rule that  $\Delta S = 0$ , this figure suggests the possibility of excitations of spin-down electrons from the naphthalene  $\pi$  orbitals to the empty d-orbitals of the copper atoms, that is, a  $\beta$ -spin  $\pi$ -d transition with a 2.195 eV gap.

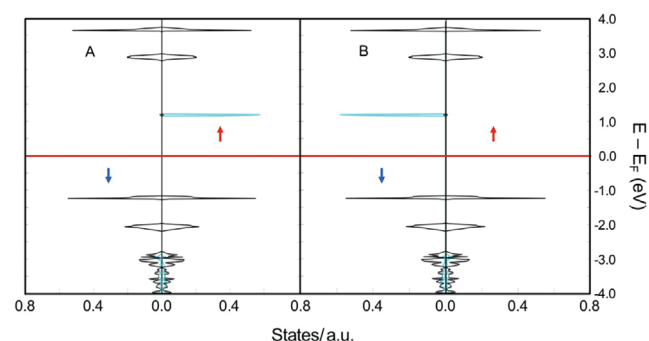


**Figure 6.** Spin-up (red arrow) and spin-down (blue arrow) projected density of states for TUB40 in the AFM configuration, showing the contributions from p-orbitals of the carbon atoms (black) and d-orbitals of the copper atoms (cyan) with an excess  $\beta$ -spin (A) and an excess  $\alpha$ -spin (B).

Our smallest calculated HOMO-LUMO gaps (namely, 2.320 and 2.195 eV) are somewhat larger than the experimental estimate of the band gap (namely, 1.42 eV). This may be due to a combination of reasons. First, our gaps were calculated at 0 K, while the experimental gap was extracted from a UV-vis spectrum obtained at room temperature. Second, the HSE06 hybrid functional that we used has a parameter that can be varied to switch between the PBE0 hybrid functional<sup>[47,48]</sup> ( $\omega = 0$ ) and the pure generalized gradient approximation PBE<sup>[49]</sup> functional (as  $\omega \rightarrow \infty$ ). Hybrid functionals include Hartree-Fock exchange, which increases long-distance interactions and, in turn, increases HOMO-LUMO gaps. Given that the default value of  $\omega = 0.11$  was used in our calculations and that our calculated HOMO-LUMO gaps overestimate the experimental one, it is possible that too much Hartree-Fock exchange was included in the functional.

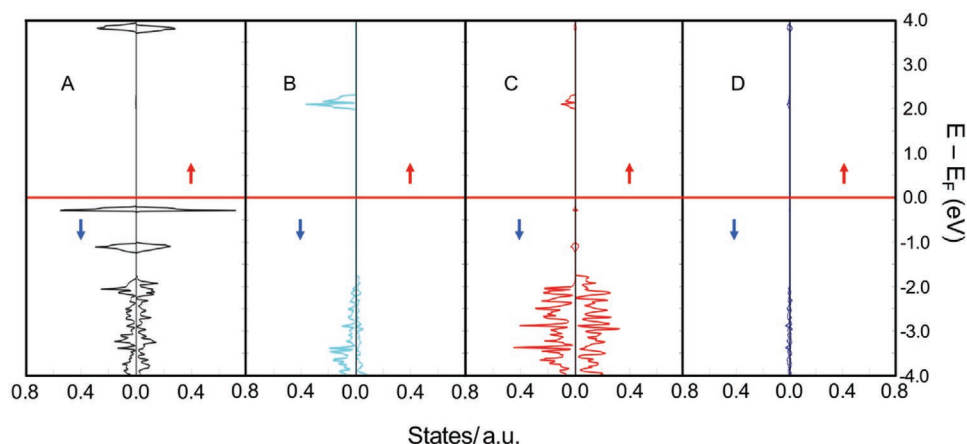


**Figure 7.** Spin-up (red arrow) and spin-down (blue arrow) projected density of states for TUB40 in the FM configuration: carbon (A), copper (B), oxygen (C), phosphorous (D).

Finally, the results of the electronic population analyses (see Table S2, Supporting Information) show that the oxygen atoms surrounding each copper atom have excess electron density (namely, for every three oxygen atoms there is approximately an excess electron), pointing to high electron delocalization within the 2D IBU. The spin density isosurface of the AFM configuration (Figure S4, Supporting Information) shows that the spin density is delocalized onto the copper atoms and oxygen atoms, suggesting that both of these atoms contribute to the magnetic behavior of TUB40.

## 5. Conclusion

In conclusion, we reported on the conductive and magnetic properties of TUB40, which is composed of 2D sheets of Cu(II)-phosphonate polyhedra. TUB40 was found to have a narrow band gap of 1.42 eV, well within the semiconducting

range. The single-crystal and pellet-based impedance measurements yielded conductivities of 200 and 142 S m<sup>-1</sup>, respectively, at room temperature, making TUB40 one of the most conductive 3D MOFs in the literature. Temperature-dependent magnetization measurements showed that the Cu(II) atoms are antiferromagnetically coupled at very low temperatures. The DFT results suggested that the electrical conduction in TUB40 is due to excitations between the spatially separated HOMO and LUMO, which are primarily located on the aromatic naphthalene rings and the Cu(II) atoms, respectively. Given their high thermal stability and extremely rich phosphonate metal-binding modes, phosphonate MOFs could become the next generation of microporous semiconductors and supercapacitor electrodes.

## Supporting Information

Supporting Information is available from the Wiley Online Library or from the author.

## Acknowledgements

G.Y. would like to thank the DFG for funding his work and DAAD for supporting B.C.'s visit to his lab at TU-Berlin. G.H. acknowledges funding from the Natural Sciences and Engineering Research Council of Canada (NSERC). The DFT calculations were enabled by support provided by WestGrid ([www.westgrid.ca](http://www.westgrid.ca)) and Compute Canada ([www.computeCanada.ca](http://www.computeCanada.ca)). The authors thank Dr. Pradip Pachfule from TU-Berlin for his help with the UV-vis measurements.

Open access funding enabled and organized by Projekt DEAL.

## Conflict of Interest

GY has a pending patent for some of the presented results. The other authors declare no conflict of interests.

## Author Contributions

D.K., F.-J.S., and P.T. contributed equally to this work. G.Y. created the hypothesis, supervised the project, and co-wrote/revised the

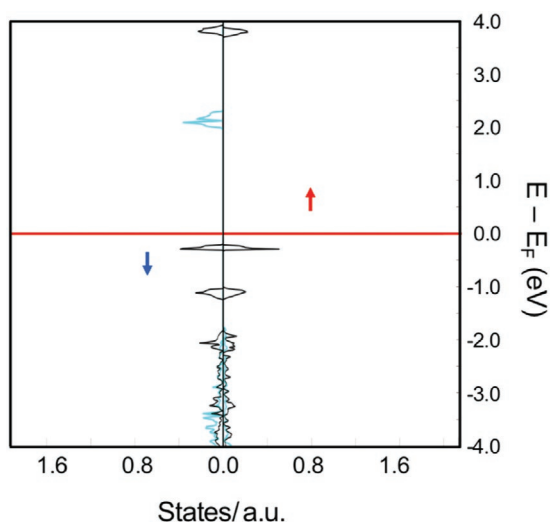


**Figure 8.** Spin-up (red arrow) and spin-down (blue arrow) projected density of states for TUB40 in the FM configuration, showing the contributions from p-orbitals of the carbon atoms (black) and d-orbitals of the copper atoms (cyan) with an excess  $\alpha$ -spin.

non-computational parts of the manuscript. P.T. resynthesized the compound and prepared the crystallographic figures. C.A.P. performed several of the DFT calculations, generated the computational figures/tables, and co-wrote the initial drafts of the computational parts of the manuscript. Q.H. performed several of the DFT calculations and co-wrote the initial draft of the computational methods section. G.H. supervised the calculations, performed extensive critical revisions of the non-computational parts of the manuscript, co-wrote the computational parts of the manuscript, and edited the entire manuscript. K.S. performed the magnetic measurements and wrote the initial drafts of the corresponding methods and results sections. B.C. prepared the Tauc plot (Figure 2A). D.K. performed the pellet-based electrical conductivity measurements and wrote the initial drafts of the corresponding methods and results sections. F.-J.S. performed the single-crystal electrical conductivity measurements. A.G. supervised D.K.'s work and provided the equipment for the electrical conductivity measurements. A.O.Y. carried out the Monte Carlo simulations for pore volume prediction.

## Keywords

electrically conductive MOFs, magnetic MOFs, phosphonate MOFs, semiconductors, supercapacitors

Received: August 28, 2020

Published online:

- [1] H. Li, M. Eddaoudi, M. O'Keeffe, O. M. Yaghi, *Nature* **1999**, 402, 276.
- [2] N. Stock, S. Biswas, *Chem. Rev.* **2012**, 112, 933.
- [3] G. Férey, C. Serre, T. Devic, G. Maurin, H. Jobic, P. L. Llewellyn, G. De Weireld, A. Vimont, M. Daturi, K. S. Chang, *Chem. Soc. Rev.* **2011**, 40, 550.
- [4] H.-C. "Joe" Zhou, S. Kitagawa, *Chem. Soc. Rev.* **2014**, 43, 5415.
- [5] A. Schneemann, V. Bon, I. Schwedler, I. Senkovska, S. Kaskel, R. A. Fischer, *Chem. Soc. Rev.* **2014**, 43, 6062.
- [6] O. M. Yaghi, M. O'Keeffe, N. W. Ockwig, H. K. Chae, M. Eddaoudi, J. Kim, *Nature* **2003**, 423, 705.
- [7] H.-C. Zhou, J. R. Long, O. M. Yaghi, *Chem. Rev.* **2012**, 112, 673.
- [8] G. Yücesan, Y. Zorlu, M. Stricker, J. Beckmann, *Coord. Chem. Rev.* **2018**, 369, 105.
- [9] C. M. Myae Soe, G. P. Nagabhushana, R. Shivaramaiah, H. Tsai, W. Nie, J. C. Blancon, F. Melkonyan, D. H. Cao, B. Traoré, L. Pedesseau, M. Kepenekian, C. Katan, J. Even, T. J. Marks, A. Navrotsky, A. D. Mohite, C. C. Stoumpos, M. G. Kanatzidis, *Proc. Natl. Acad. Sci. USA* **2019**, 116, 58.
- [10] Q. Tai, K. C. Tang, F. Yan, *Energy Environ. Sci.* **2019**, 12, 2375.
- [11] A. E. Baumann, D. A. Burns, B. Liu, V. S. Thoi, *Commun. Chem.* **2019**, 2, 86.
- [12] L. Sun, M. G. Campbell, M. Dincă, *Angew. Chem., Int. Ed.* **2016**, 55, 3566.
- [13] D. Sheberla, J. C. Bachman, J. S. Elias, C. J. Sun, Y. Shao-Horn, M. Dincă, *Nat. Mater.* **2017**, 16, 220.
- [14] C. Yang, R. Dong, M. Wang, P. S. Petkov, Z. Zhang, M. Wang, P. Han, M. Ballabio, S. A. Bräuningner, Z. Liao, J. Zhang, F. Schwotzer, E. Zschech, H.-H. Klaus, E. Cánovas, S. Kaskel, M. Bonn, S. Zhou, T. Heine, X. Feng, *Nat. Commun.* **2019**, 10, 3260.
- [15] K. Siemensemeyer, C. A. Peeples, P. Tholen, F. J. Schmitt, B. Çoşut, G. Hanna, G. Yücesan, *Adv. Mater.* **2020**, 32, 2000474.
- [16] L. S. Xie, G. Skorupskii, M. Dincă, *Chem. Rev.* **2020**, 120, 8536.
- [17] O. K. Farha, I. Eryazici, N. C. Jeong, B. G. Hauser, C. E. Wilmer, A. A. Sarjeant, R. Q. Snurr, S. T. Nguyen, A. Ö. Yazaydin, J. T. Hupp, *J. Am. Chem. Soc.* **2012**, 134, 15016.
- [18] R. Grönker, V. Bon, P. Müller, U. Stoeck, S. Krause, U. Mueller, I. Senkovska, S. Kaskel, *Chem. Commun.* **2014**, 50, 3450.
- [19] I. M. Hönicke, I. Senkovska, V. Bon, I. A. Baburin, N. Bönisch, S. Raschke, J. D. Evans, S. Kaskel, *Angew. Chem., Int. Ed.* **2018**, 57, 13780.
- [20] P. Tholen, Y. Zorlu, J. Beckmann, G. Yücesan, *Eur. J. Inorg. Chem.* **2020**, 2020, 1542.
- [21] M. Taddei, G. M. Schukraft, M. E. A. Warwick, D. Tiana, M. J. McPherson, D. R. Jones, C. Petit, *J. Mater. Chem. A* **2019**, 7, 23781.
- [22] X. P. Wu, L. Gagliardi, D. G. Truhlar, *J. Am. Chem. Soc.* **2018**, 140, 7904.
- [23] K. AlKaabi, C. R. Wade, M. Dincă, *Chem* **2016**, 1, 264.
- [24] J. G. Park, M. L. Aubrey, J. Oktawiec, K. Chakarawet, L. E. Darago, F. Grandjean, G. J. Long, J. R. Long, *J. Am. Chem. Soc.* **2018**, 140, 8526.
- [25] M. Kurmoo, *Chem. Soc. Rev.* **2009**, 38, 1353.
- [26] G. M. Espallargas, E. Coronado, *Chem. Soc. Rev.* **2018**, 47, 533.
- [27] Y. Zorlu, D. Erbahar, A. Çetinkaya, A. Bulut, T. S. Erkal, A. O. Yazaydin, J. Beckmann, G. Yücesan, *Chem. Commun.* **2019**, 55, 3053.
- [28] K. J. Gagnon, H. P. Perry, A. Clearfield, *Chem. Rev.* **2012**, 112, 1034.
- [29] S. J. I. Shearan, N. Stock, F. Emmerling, J. Demel, P. A. Wright, K. D. Demadis, M. Vassaki, F. Costantino, R. Vivani, S. Sallard, I. R. Salcedo, A. Cabeza, M. Taddei, *Crystals* **2019**, 9, 270.
- [30] R. A. Coxall, S. G. Harris, D. K. Henderson, S. Parsons, P. A. Tasker, R. E. P. Winpenny, *J. Chem. Soc., Dalton Trans.* **2000**, 2349.
- [31] D. Sahoo, R. Suriyanarayanan, V. Chandrasekhar, *Dalton Trans.* **2014**, 43, 10898.
- [32] A. Bulut, Y. Zorlu, M. Wörle, S. Paşa, H. Kurt, J. Zubieta, J. Beckmann, G. Yücesan, *Eur. J. Inorg. Chem.* **2016**, 2016, 3506.
- [33] *Metal Phosphonate Chemistry: From Synthesis to Applications*, (Eds: A. Clearfield, K. Demadis), Royal Society of Chemistry, Cambridge, UK **2011**.
- [34] R. J. Motekaitis, I. Muráse, A. E. Martell, *Inorg. Chem.* **1976**, 15, 2303.
- [35] I. R. Salcedo, R. M. P. Colodrero, M. Bazaga-García, A. Vasileiou, M. Papadaki, P. Olivera-Pastor, A. Infantes-Molina, E. R. Losilla, G. Mezei, A. Cabeza, K. D. Demadis, *CrystEngComm* **2018**, 20, 7648.
- [36] C. Y. Gao, J. Ai, H. R. Tian, D. Wu, Z. M. Sun, *Chem. Commun.* **2017**, 53, 1293.
- [37] Z. Amghouz, J. R. García, S. García-Granda, A. Clearfield, J. R. Fernández, I. De Pedro, J. A. Blanco, *J. Alloys Compd.* **2012**, 536, S499.
- [38] N. R. Dhineshbabu, V. Rajendran, N. Nithyavathy, R. Vetumperumal, *Appl. Nanosci.* **2016**, 6, 933.
- [39] P. Grima-Gallardo, M. Salas, O. Contreras, C. Power, M. Quintero, H. Cabrera, I. Zumeta-Dubé, A. Rodríguez, J. Aitken, W. Brämer-Escamilla, *J. Alloys Compd.* **2016**, 658, 749.
- [40] J. Tauc, R. Grigorovici, A. Vancu, *Physica Status Solidi* **1966**, 15, 627.
- [41] L. Lederová, A. Orendáčová, J. Chovan, J. Strečka, T. Verkholyak, R. Tarasenko, D. Legut, R. Sýkora, E. Čižmár, V. Tkáč, M. Orendáč, A. Feher, *Phys. Rev. B* **2017**, 95, 054436.
- [42] J. A. Mydosh, *Handbook of Magnetic Materials*, Vol. 10, North-Holland, Amsterdam, The Netherlands **1997**.
- [43] E. Pellicer, A. Varea, S. Pané, B. J. Nelson, E. Menéndez, M. Estrader, S. Suriñach, M. D. Baró, J. Nogués, J. Sort, *Adv. Funct. Mater.* **2010**, 20, 983.
- [44] W. Li, L. Sun, J. Qi, P. Jarillo-Herrero, M. Dincă, J. Li, *Chem. Sci.* **2017**, 8, 2859.
- [45] R. A. De Groot, F. M. Mueller, P. G. V. Engen, K. H. J. Buschow, *Phys. Rev. Lett.* **1983**, 50, 2024.
- [46] J. M. D. Coey, M. Venkatesan, *J. Appl. Phys.* **2002**, 91, 8345.
- [47] C. Adamo, V. Barone, *J. Chem. Phys.* **1999**, 110, 6158.
- [48] M. Ernzerhof, G. E. Scuseria, *J. Chem. Phys.* **1999**, 110, 5029.
- [49] J. Perdew, K. Burke, M. Ernzerhof, *Phys. Rev. Lett.* **1996**, 77, 3865.